International Journal of the Physical Sciences Vol. 6(33), pp. 7638 - 7650, 9 December, 2011
Available online at http://www.academicjournals.org/IJPS
DOI: 10.5897/IJPS11.910
ISSN 1992 - 1950 ©2011 Academic Journals

Full Length Research Paper

The Earth Observing-1 (EO-1) satellite data for geological mapping, southeastern segment of the Central Iranian Volcanic Belt, Iran

Amin Beiranvand Pour and Mazlan Hashim*

Institute of Geospatial Science and Technology (INSTeG), Universiti Teknologi Malaysia, 81310 UTM Skudai, Johor Bahru, Malaysia.

Accepted 14 November, 2011

This investigation used Earth Observing-1 (EO-1) ALI (advanced land imager) and hyperion data to extract the geological and mineralogical information for identifying hydrothermal alteration zones associated with porphyry copper deposits in southeastern segment of the Central Iranian Volcanic Belt, SE Iran. A band ratio derived from image spectra (4/2, 8/9, 3 in RGB) has been developed to identify lithological units and hydrothermally altered rocks using ALI data in a regional scale. Analytical imaging and geophysics (AIG)-Developed Hyperspectral Analysis processing methods were tested on the shortwave infrared bands of hyperion for mapping mineral assemblages in hydrothermal alteration zones associated with two known copper ore deposits, namely Sar Cheshmeh and Meiduk. The methods produced image map of spectrally predominant minerals in alteration zones using hyperion data. Therefore, phyllic, argillic, and propylitic alteration zones were significantly discriminated from surrounding country rock. The spatial distribution of identified hydrothermal alteration zones has been confirmed by spectral reflectance measurements, XRD analysis and *in-situ* inspection. The research presented here indicated that lithological units, hydrothermally altered rocks, and hydrothermal alteration zones associated with porphyry copper mineralization can be accurately mapped by ALI and hyperion data at both regional and district scales.

Key words: Advanced land imager (ALI), hyperion, analytical imaging and geophysics (AIG)-developed hyperspectral analysis processing methods, Central Iranian Volcanic Belt.

INTRODUCTION

The Earth Observing-1 (EO-1) satellite was launched on 21 November of 2000 as part of NASA's New Millennuim Program (NMP) technology path-finding activities to enable more effective (and less costly) hardware and strategies for meeting earth science mission needs in the 21st century. The EO-1 satellite contains three observing instruments supported by a variety of newly developed space technologies (Unger et al., 2003). It includes three of the most advanced remote sensing sensors: (1) The advanced land imager (ALI); (2) Hyperion; and (3) The linear etalon imaging spectral array (LEISA) atmospheric corrector (LAC). These sensors can be used in a variety of scientific disciplines (Beck, 2003; Ungar et al., 2003).

The advanced land imager (ALI) is a prototype for a new generation of Landsat-7 Thematic Mapper. The sensor maintains similar characteristics to Landsat-7 with a spatial resolution of 30 m; however, the swath width is 37 km as opposed to 185 km (Hearn et al., 2001; National Aeronautics and Space Administration, 2002; Wulder et al., 2008). It includes detector arrays that operate in ten bands, one panchromatic, six in visible and near infrared radiation (VNIR), and three in shortwave infrared radiation (SWIR), spanning the range from 0.433 to 2.35 µm. The performance characteristics of the ALI

*Corresponding author. E-mail:mazlanhashim@utm.my, profmhashim@gmail.com. Tel: +607 -5530666. Fax: +607-5531174.

Table 1. The performance characteristics of the ALI and ETM+ sensors (Beck, 2003).

Sensor	Subsystem	Band number	Spectra range (μm)	Ground resolution (m)	Swath width (km)	Temporal resolution
ALI	VNIR	Pan	0.480-0.690	10	37	16 days
		1	0.433-0.453	30		
		2	0.450-0.515			
		3	0.525-0.605			
		4	0.633-0.690			
		5	0.775-0.805			
		6	0.845-0.890			
	SWIR	7	1.200-1.300			
		8	1.550-1.750			
		9	2.080-2.350			
ETM+	VNIR	Pan	0.520-0.900	14.25	185	16 days
		1	0.450-0.515	28.50		
		2	0.525-0.605			
		3	0.633-0.690			
		4	0.780-0.900			
	SWIR	5	1.550-1.750			
		7	2.090-2.350			
	TIR	6	10.45-12.50			

Table 2. The performance characteristics of the hyperion sensor (Folkman et al., 2001).

Sensor	Subsystem	Band number	spectral range (μm)	Ground resolution (m)	Swath width (km)	Radiometric precision (S/N)
Hyperion	VNIR	Continuous	0.400-1.000	30	7.6	161/1
	SWIR	Continuous	0.900-2.500	30	7.6	40/1

and ETM+ are shown in Table 1.

Hyperion is the first advanced satellite hypersepctral sensor operating across the full solar-reflected spectrum with nominal spectral coverage from 0.4 to 2.5 μm and 10 nm spectral resolution. It is a push broom instrument, capturing 256 spectra each with 242 spectral bands over a 7.6 km swath width and 30 m spatial resolution. The 242 total bands include the first 70 bands in the visible and near infrared region and the second 172 bands in the shortwave infrared region (Beck, 2003; Pearlman et al., 2003; Unger et al., 2003). The performance characteristics of Hyperion are shown in Table 2. Hyperion shortwave infrared bands (2.0 to 2.5 μm) can uniquely identify and map hydroxyl-bearing minerals, sulfates, and carbonates in the hydrothermal alteration assemblages (kruse et al., 2003).

Spectral information extraction from ALI and hyperion data has great ability to assist geologists for geological mapping and exploring high economic-potential copper and gold mineralization zones in arid and semi-arid regions. This study investigates the potential values of spectral information extraction of the advanced land imager (ALI) and hyperion remote sensing data for geological mapping in a semi-arid territory in the south-eastern segment of the NW-SE trending Central Iranian Volcanic Belt (Figure 1). In this belt, the abundance of known and mined porphyry copper and gold deposits reflects its economic potential, which warrants the exploration for new and additional prospects. Yearly precipitation averages very low especially in the southeastern belt segment, thus the deposit's exposure is well due to sparse and nonexistent vegetation cover, which makes this sit quite suitable for our remote sensing analysis. Our image analyses focuses on the Meiduk and Sarcheshmeh porphyry copper deposits, which are located in the southeastern part of the Urumieh-Dokhtar

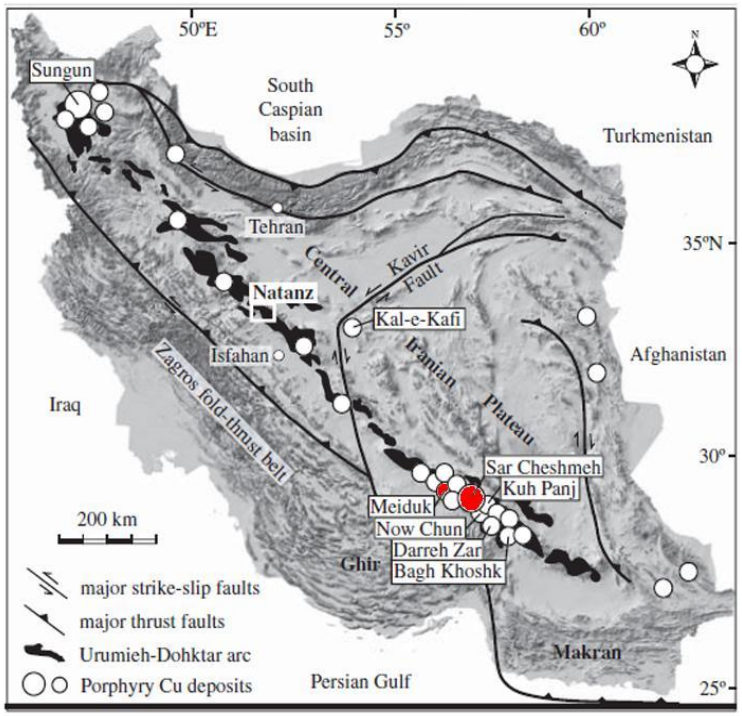

Figure 1. (a) Location of the Central Iranian volcanic belt and distribution of porphyry Cu deposits in Iran. (b) Simplified litho-structural map of the southeastern of the volcanic belt and location of major porphyry Cu deposits and prospects (modified from Shafiei, 2010). Study areas are located in red circles.

volcanic belt, SE Iran, where Cu and Mo are actively being mined. As the literature admits, in recent years, few remote sensing studies were carried out in the study area using ASTER data (Pour et al., 2011; Pour and Hashim, 2011a, b; Ranjbar et al., 2011). This study tested analytical imaging and geophysics (AIG)-developed hyperspectral analysis processing methods over shortwave infrared radiation (SWIR) bands of hyperion to extract spectral information for mineralogical mapping at district scale. A band ratio derived from image spectra has been developed to map hydrothermally altered rocks using ALI data at regional scale.

REGIONAL GEOLOGIC SETTING

The central Iran, Southeastern Turkey, Southern Pamir and Arabia and Central Afghanistan were part of Gondwanaland from Late Precambrian until Late Paleozoic time, separated from the Eurasian plate by the Paleo-tethys Ocean. The closure of Paleo-tethys during Triassic time by the northward motion of these micro-continents resulted in their welding with the Eurasian plate along a suture zone. The Late Paleozoic ophiolites were emplaced in the north in the Middle Triassic, probably at the time of collision of continental fragments with the Eurasian plate.

Accordingly, Eurasia appears to have grown from the Middle to Late Triassic by successive accretion of micro-continents which came from the south, across the Tethyan seaway. Approximately, rifting along the present Zagros thrust zone of the continental plate took place, at the same time during the closure of Paleo-tethys in the north, resulting in the opening of a new ocean called Neo-tethys. The floor of Neo-tethys started to subduct beneath the Eurasian plate with the disappearance of Paleo-tethys during Triassic-Jurassic time. This conducted to an Early Cimmerian metamorphic event, recorded in the Southwest Sanandaj-Sirjan zone (Alavi, 1994; Shahabpour, 2005), and also Upper Triassic emplacement of intrusive bodies. The final closure of Neo-tethys and collision between Arabian and Iranian micro-plate took place during the Neogene that followed by collision of the Arabian and Eurasian plates which formed the Central Iranian Volcanic Belt during the Alpine orogeny (Berberian et al., 1982).

The Central Iranian Volcanic Belt is a volcano-plutonic complex which contains extrusive and intrusive rocks of Eocene to Quaternary age. Geochemical investigations have shown that this volcanic belt is generally consists of subduction-related calc-alkaline rocks (Berberian et al., 1982; Shahabpour, 2005, 2007). In this belt, mountains

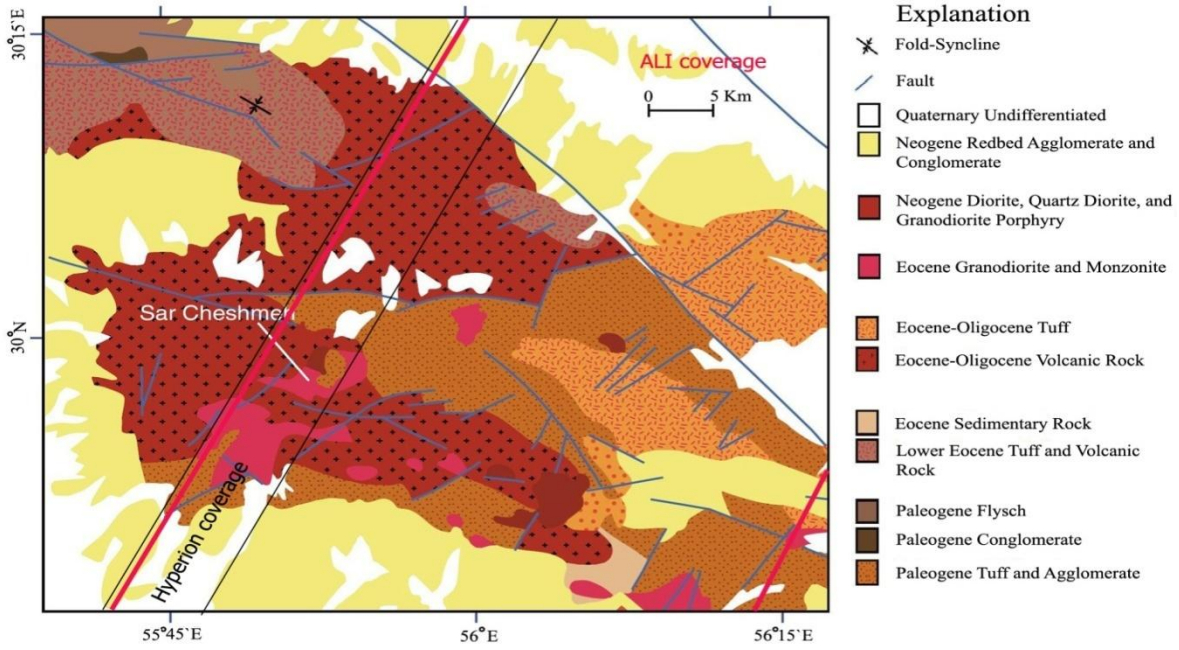

Figure 2. Geological map of the Sarcheshmeh region (Modified from Hubner, 1969a; Mars and Rowan, 2006) and EO1 coverage data. Black lines show the hyperion coverage; red lines show the ALI coverage.

include a volcanic succession of Eocene calc-alkaline basaltic andesite and oligocene shoshonitic rocks intruded by Neogene quartz diorites, quartz monzonites, and granodiorites which contain vein type and porphyry copper mineralization (Hubner, 1969a; Hassanzadeh, 1993). The most of volcanism occurred from Eocene to Miocene time in this belt (Hubner, 1969a).

Extensive mineralization occurred from Miocene to Pliocene time and produced porphyry copper and vein-type mineralization. Porphyry copper deposits in this belt are associated with Miocene adakite-like orogenic granitoids which intruded the Eocene volcanic rocks (Shafiei et al., 2009). Giant porphyry copper ore deposits in this belt, including Sarcheshmeh and Meiduk are in a granodiorite and a quartz diorite pluton, respectively (Hassanzadeh, 1993). Most of the porphyry copper deposits are associated with well developed potassic (K-feldspar and biotite), sodic (albite), sericitic, silicic, propylitic, and locally argillic alteration. Mineralization occurs as quartz stockworks, veins and disseminated sulfides in both the Miocene porphyritic stocks and the Eocene mafic and intermediate volcanic rocks. Common hypogene ore minerals are chalcopyrite and pyrite with subordinate molybdenite, bornite, and magnetite. Supergene oxidation and secondary Cu-enrichment occurred in all the deposits, but are well developed only in the giant and largest deposits such as Sarcheshmeh and Meiduk (Shafiei, 2010).

The Sarcheshmeh porphyry copper deposit (55° 52′ 20″ E, 29° 58′ 40″ N) is located 160 Km southwest of Kerman city. The deposit is within a belt of Eocene volcanic rocks and Oligo-Miocene subvolcanic granitoid rocks (Waterman and Hamilton, 1975) (Figure 2). The oldest host rocks at the Sarcheshmeh porphyry copper deposit belong to an Eocene volcanogenic complex, also known as the Sarcheshmeh complex. The complex consists of pyroxene trachybasalt, pyroxene trachyandesite of potassic and shoshonitic affinity, less abundant andesite and rare occurrences of agglomerate, tuff, and tuffaceous sandstone.

Hydrothermal alteration and mineralization at Sarcheshmeh are centered on the stock and were broadly synchronous with its emplacement. Early hydrothermal alteration was dominantly potassic and propylitic, and was followed later by phyllic, silicic and argillic alteration (Hezarkhani, 2006).

The Meiduk porphyry copper deposit (55° 10′ 05″ E, 30° 25′ 10″ N) is located 45 km northeast of Shahr-e-Babak city. Figure 3 shows geological map of the Meiduk area. The deposit is hosted by Eocene andesitic and basaltic rocks, changing sequentially to conformable south dipping Eocene red tuffs and tuffaceous sediments, trachyandesite and trachybasalts, trachyandesitic and trachybasaltic lava flows and porphyrites to the southwest. The Cu-mineralization and associated hydrothermal alteration zones are focused on the Miocene dioritic Meiduk porphyry and Eocene andesitic rocks (Boomeri et al., 2009). Amiraie, (1991) recognized potassic, phyllic, argillic, and propylitic alteration zones at Meiduk area.

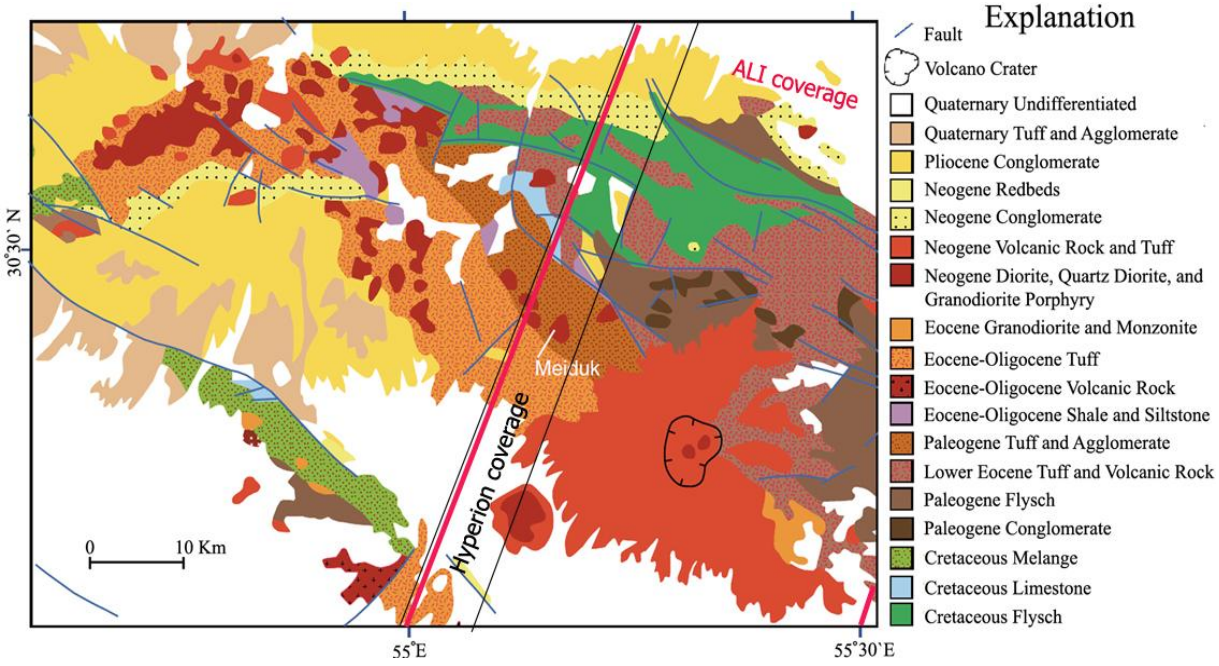

Figure 3. Geological map of the Meiduk region (Modified from Hubner, 1969b; Mars and Rowan, 2006) and EO1 coverage data. Black lines show the hyperion coverage; red lines show the ALI coverage.

Shortwave Infrared (SWIR) remote sensing data for alteration mineral mapping

The shortwave infrared (SWIR) radiation is the best spectral region of the electromagnetic spectrum for sensing various aspects of hydrothermal alteration zones. Hydroxyl-bearing minerals including clay and sulfate groups as well as carbonate minerals present diagnostic spectral absorption features due to vibrational processes of fundamental absorptions of Al–O–H, Mg–O–H, Si–O–H, and CO_3 groups in the shortwave infrared radiation region, and thus this wavelength region is the best to explore and typify hydrothermal alteration systems (Huntington, 1996). The primary objective in this wavelength region is to map the spatial distribution of hydrothermal alteration minerals containing OH groups. Phyllosilicates including Al-Si-(OH) and Mg-Si-(OH) bearing minerals such as kaolinite, montmorillonite, muscovite, illite, talc, chlorite and sorosilicate group including Ca-Al-Si-(OH) bearing minerals such as epidote group and OH-bearing sulfates including alunite and gypsum, and also carbonates can be identified by virtue of their spectral characteristics in shortwave infrared radiation region (Hunt, 1977; Hunt and Ashley, 1979). Therefore, the remote sensing shortwave infrared radiation data can be used for the identification of hydrothermal alteration mineral assemblages including: (1) Mineralogy generated by the passage of low pH fluids (alunite and pyrophylite); (2) Al-Si-(OH) and Mg-Si-(OH)-bearing minerals including kaolinite and mica and chlorite groups; and (3) Ca-Al-Si-(OH) bearing minerals such as epidote group, as well as carbonate group (calcite and dolomite). Previous studies have demonstrated the identification of specific hydrothermal alteration minerals, such as alunite, kaolinite, calcite, dolomite, chlorite, talc and muscovite, as well as mineral groups, through analysis of multispectral and hyperspectral shortwave infrared radiation data, which have been proven using *in situ* field spectral measurements (kruse et al., 2003; Mars and Rowan, 2006; Gersman et al., 2008).

MATERIALS AND METHODS

Remote sensing data

ALI and hyperion images were acquired through the U.S. Geological Survey Earth Resources Observation System (EROS) Data center (EDC). Two cloud-free level 1B ALI and hyperion scenes were collected over Meiduk on August 18, 2004 and Sarcheshmeh area on September 14, 2010, respectively. The images were pre-georeferenced to UTM zone 40 North projection with WGS-84 datum.

Preprocessing of remote sensing data

Hyperion level 1B has a total of 242 bands but only 198 bands are calibrated. Because of an overlap between the VNIR and SWIR focal planes, only 196 unique channels can be considered for further processing (Beck, 2003). Spectral bands covering the shortwave infrared spectral range (2.0 to 2.4 µm) were selected in this study. Preprocessing was involved destriping and atmospheric

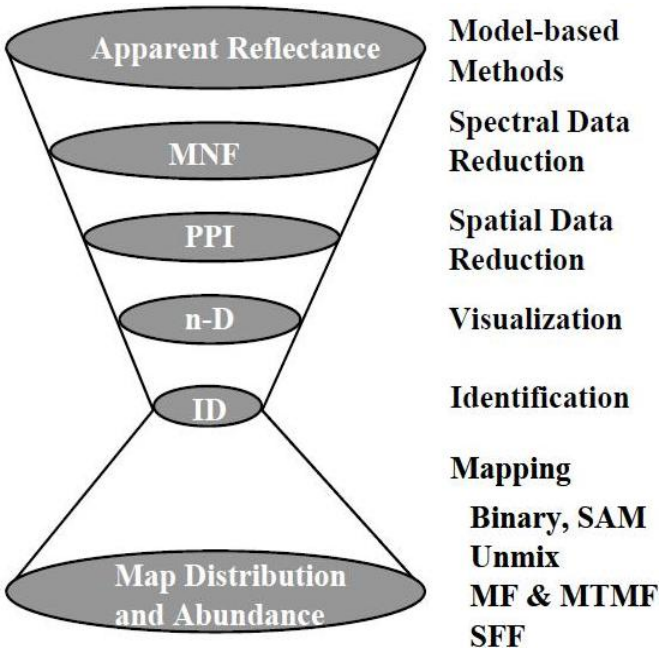

Figure 4. AGI processing methods for hyperspectral data analysis (Kruse et al., 2003).

correction. After radiometric corrections, there is still a pronounced vertical striping pattern in the hyperion data, such striping is often seen in data acquired using pushbroom technology (Kruse et al., 2003). Desteriping of the hyperion Level 1B data was accomplished before atmospheric correction. To correct the atmospheric effects, Atmospheric CORrection Now (ACORN) software was used to retrieve the surface reflectance (Kruse et al., 2003; ACORN^{TM} 5.0, 2004). During the atmospheric correction, raw radiance data from imaging spectrometer is re-scaled to reflectance data. ALI Level 1B data converted to surface reflectance using ACORN software.

Image processing methods

Band ratio is a method where the digital number value of one band is divided by the digital number value of another band. Band ratios are very useful for highlighting certain features or materials that cannot be seen in the raw bands (Inzana et al., 2003). High digital number values in the scene indicate spectral signatures similar to those of the particular materials (minerals); they were designed to map (Gad and Kusky, 2007; Rockwell and Hofstra, 2008).

Analytical imaging and geophysics (AIG)-developed hyper-spectral analysis methods was developed by Kruse and Boardman (2000) and associates at analytical imaging and geophysics LLC (AIG) for analysis of hyperspectral data. Data are analyzed using AIG approach to determine unique spectral end-members and their spatial distribution, abundances, and producing detailed mineral maps (Kruse et al., 2003). These methods derive the maximum information from the hyperspectral data and minimizing the reliance on a priori or outside information (Kruse and Perry, 2007). The analysis approach consists of the following steps: (1) Spectral compression, noise suppression, and dimensionality reduction using the minimum noise fraction (MNF) transformation (Green et al., 1988; Boardman, 1993); (2) Spatial data reduction using the pixel purity index (PPI) (Boardman, 1993); (3) Extraction of end-member spectra using *n*-Dimensional Visualizer (Boardman, 1993; (4) Identification of end-member spectra using visual inspection, automated identification, and spectral library comparisons (Kruse et al., 1993); and (5) Production of material maps using a variety of spectral mapping methods (Figure 4). AIG-Developed Hyperspectral Analysis processing methods were tested to shortwave infrared radiation (SWIR) bands of ALI and selected Hyperion bands include 185 to 222 covering 2.0 to 2.4 µm of the SWIR region for hydrothermally altered rock mapping and the detection of predominant mineral assemblages in hydrothermal alteration zones associated with porphyry copper mineralization at both regional and district scales. Hyperion and ALI data were processed by ENVI (Environment for Visualizing Images) version 4.5 software package.

RESULTS AND DISCUSSION

As the first step towards the identification of hydrothermal alteration minerals using ALI data, band ratios were created based on laboratory spectra of the minerals related with hydrothermal alteration. Mapping iron oxides is carried out using bands 2 and 4 of ALI because iron oxide/hydroxide minerals such as hematite, jarosite and limonite have high reflectance within 0.63 to 0.69 µm (the equivalent to ETM+ band 3) and high absorption within 0.45 to 0.52 µm (the equivalent to ETM+ band 1). The analysis to map clay minerals must incorporate bands 8 and 9 of ALI attributed to high reflectance in the range of 1.55 to 1.75 µm and high absorption in 2.08 to 2.35 µm that correspond with ETM+ bands 5 and 7, respectively. Accordingly, a band ratio derived from image spectra (4/2, 8/9, 3 in RGB) has been developed. This band ratio allows the identification of altered rocks, lithological units and vegetation. The altered rocks are outlined in the images where they appear as yellow to whitish yellow color. We have highlighted the known and mined copper deposits and identified prospects by their names in Figures 5 and 6. Vegetation is manifested as light green, and lithological units are identifiable in both ALI scenes (Figures 5 and 6).

SWIR bands hyperion bands consist of 185 to 222 that cover spectral range 2.0 to 2.4 of shortwave infrared region were selected for applying AIG approach. These bands were linearly transformed using the minimum noise fraction (MNF) transformation. The Bands 1 to 3 of two dataset were selected as input data considering the higher Eigenvalues, because MNF component images show steadily decreasing image quality with increasing component number (Chen, 2000). Hence, higher Eigenvalues generally have higher spectral information content.

Figure 7 indicate plot of the MNF Eigenvalues and MNF bands for the transformed dataset of hyperion data. As a result, only a subset of three selected MNF bands was maintained for subsequent processing in this study.

MNF Bands 1 to 3 were assigned to RGB color composites. Figures 8 and 9 illustrate RGB color composites of MNF Bands 1 to 3 for hyperion data. Figure 8 shows hydrothermally altered rocks as yellow

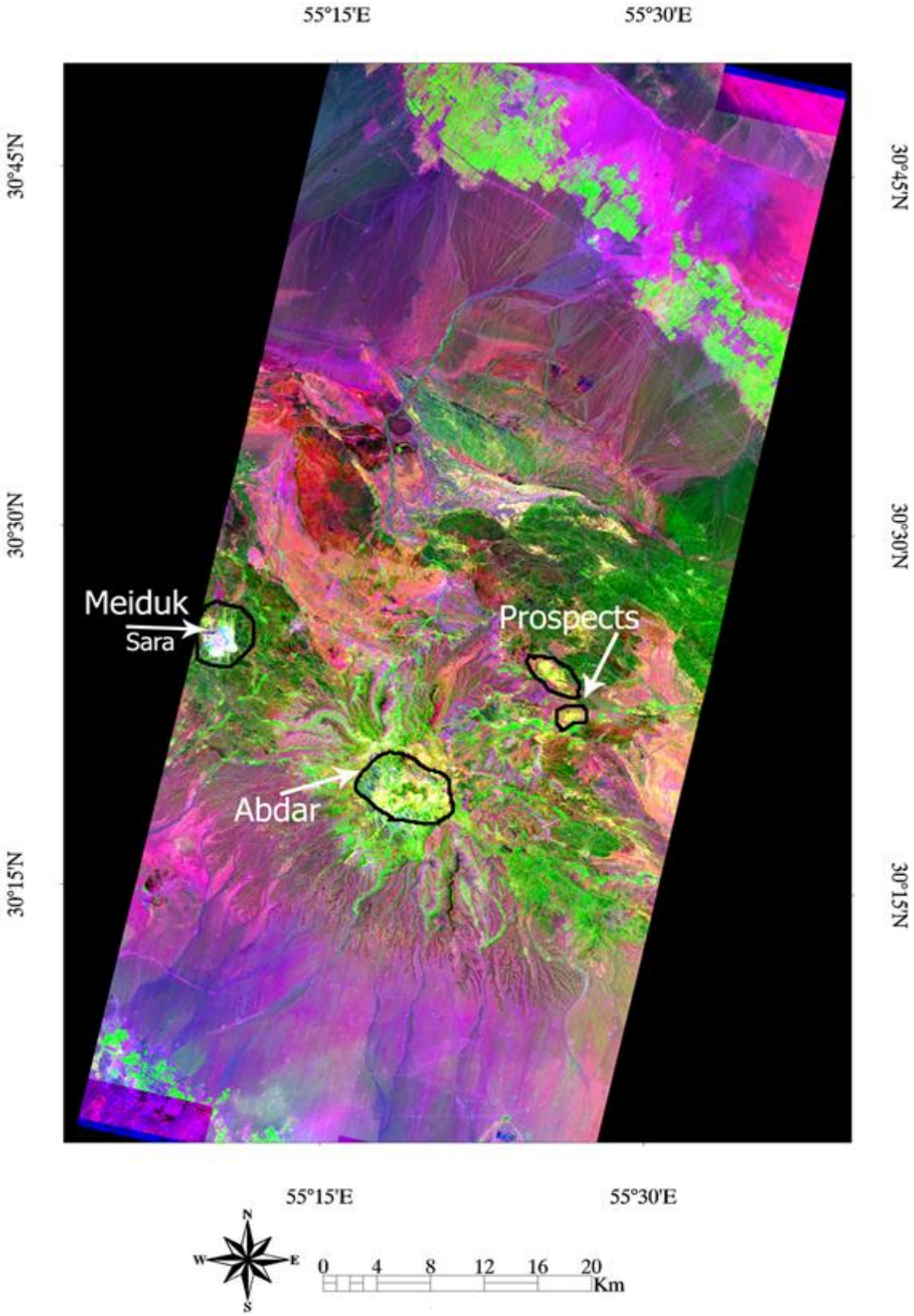

Figure 5. Band ratio of 4/2, 8/9, 3 in RGB derived from ALI bands show altered rocks as yellow to whitish yellow color. Vegetation manifests as light green color, and lithological units are recognizable in the Meiduk ALI scene.

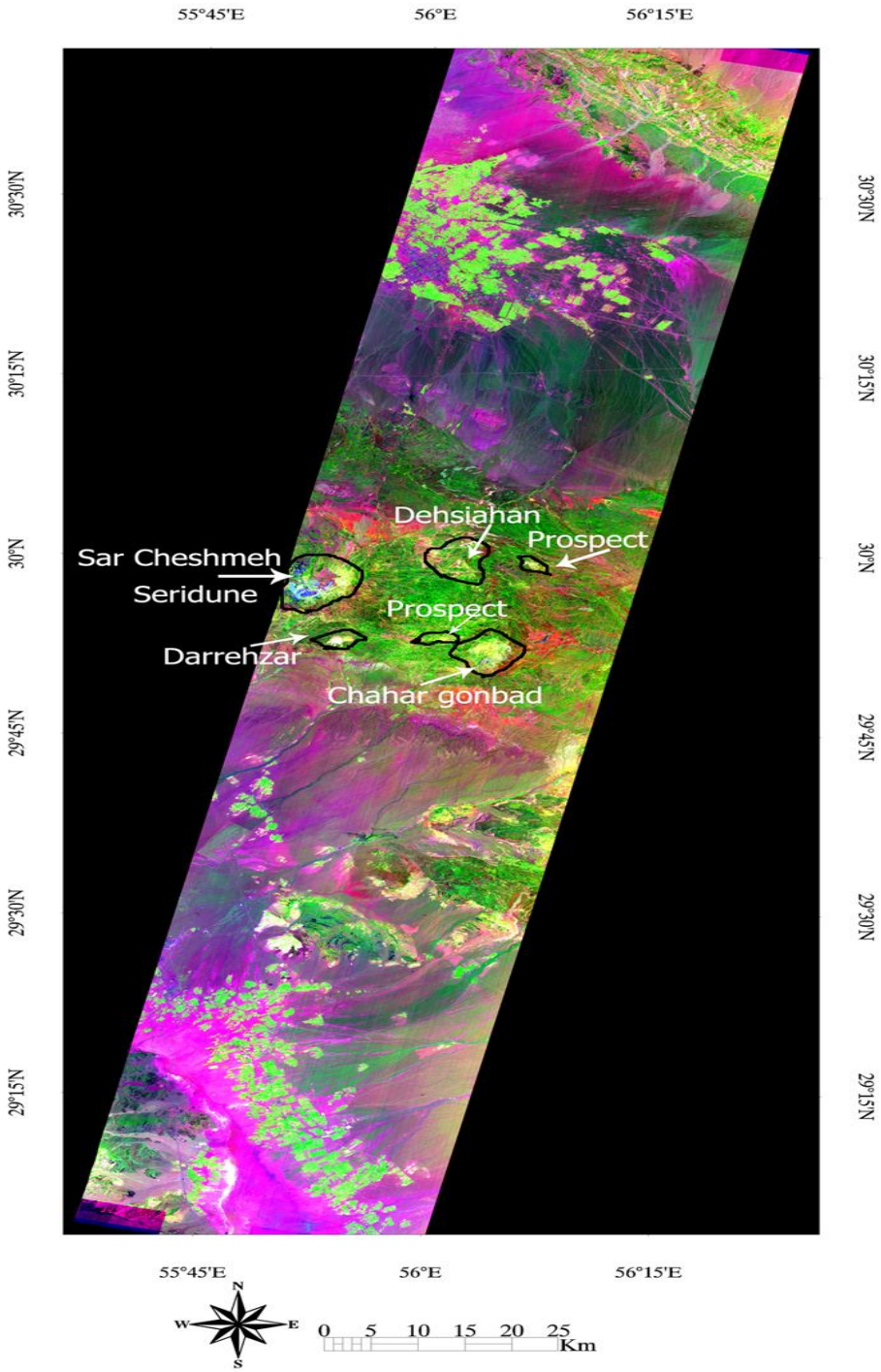

Figure 6. Band ratio of 4/2, 8/9, 3 in RGB derived from ALI bands show altered rocks as yellow to whitish yellow color. Vegetation manifests as light green color, and lithological units are recognizable in the Sar Cheshmeh ALI scene.

and green colors around Sarcheshmeh and Seridun mines. In the Figure 8, hydrothermally altered rocks manifested as white and light green colors around Meiduk mine and Sara prospect.

Three of top MNF transformed bands, which contain most of the spectral information, were used to determine the most likely end-members using pixel purity index (PPI) procedure. These potential end-member spectra

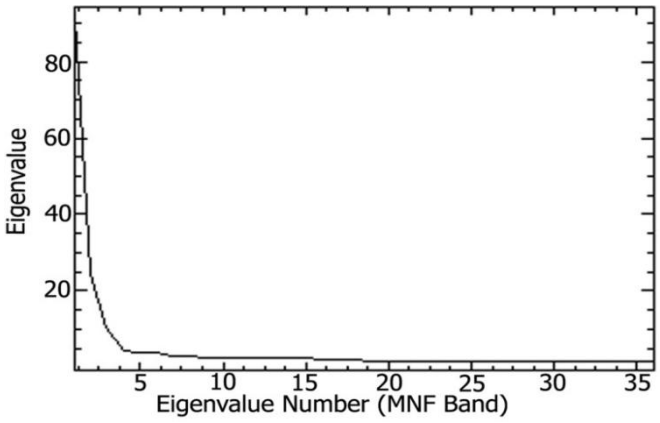

Figure 7. MNF Eigenvalue plot for selected bands of hyperion data.

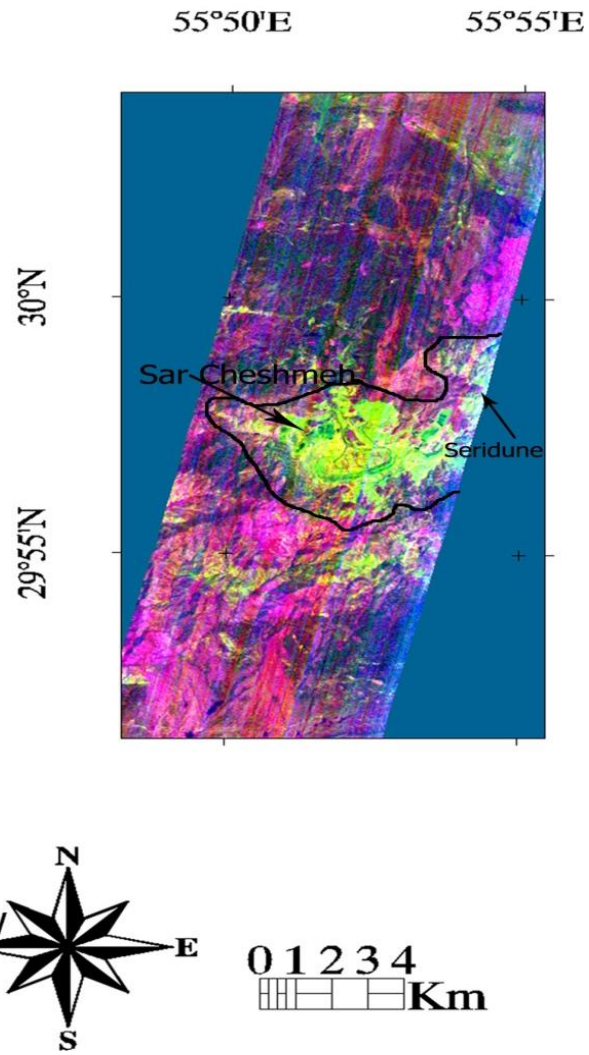

Figure 8. RGB color composites of MNF Bands 1, 2, and 3 extracted from hyperion selected bands. Yellow and green colors show hydrothermally altered rocks around Sarcheshmeh and Seridun mines.

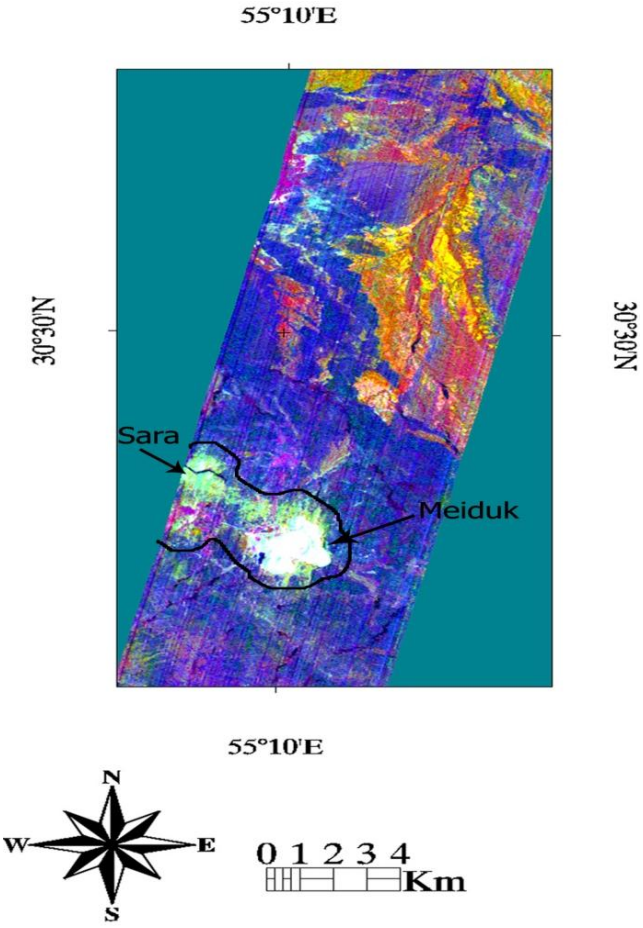

Figure 9. RGB color composites of MNF Bands 1, 2 and 3 extracted from hyperion selected bands. White and light green colors show hydrothermal altered rocks around Meiduk mine and Sara prospect.

were then loaded into an *n*-dimensional (*n*-D) scatter plot and rotated in real time on the computer screen until "points" or extremities on the scatterplot were exposed (Boardman, 1993).

These projections were "painted" using region-of-interest (ROI) definition procedures and then rotated again in three dimensions to determine their signatures that were unique in the MNF data. While this portion of the analysis presents the greatest opportunity for subjective bias, iterative *n*-D rotation and examination of remaining data dimensionality after selection of each subsequent end-member minimizes this effect and maximizes the chance of reproducible results. Once a set of unique pixels was defined using the *n*-D analysis technique, then each separate projection on the scatter plot (corresponding to a pure end-member) was exported to a ROI in the image.

Mean spectra were then extracted for each ROI from the apparent reflectance data to act as end-members for spectral mapping (Kruse et al., 2003). The extracted end-

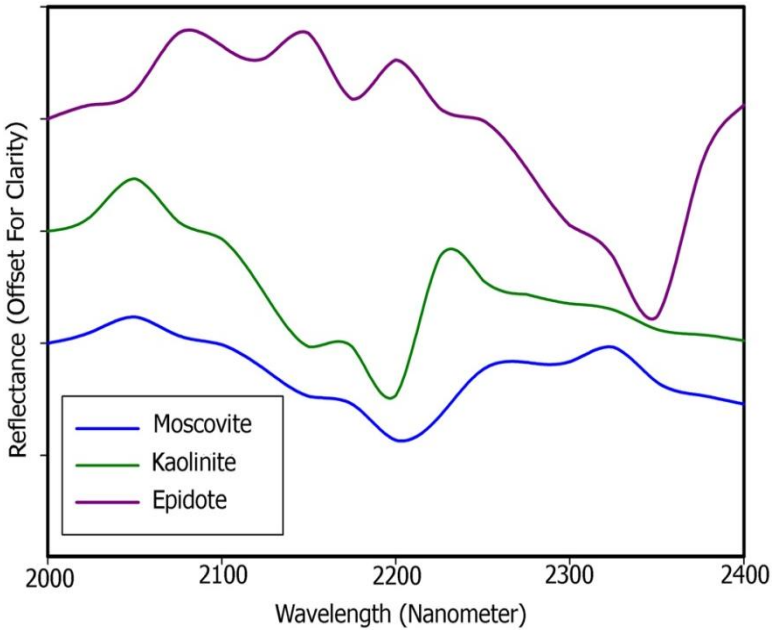

Figure 10. Selected end-member (mean) spectra extracted from SWIR (2.0 to 2.4 µm) hyperion data for the Meiduk and Sarcheshmeh sites.

members from the image processing methods were then compared to known spectra from USGS spectral libraries for identification.

A subset of identified end-member spectra that extracted from the hyperion data was used for spectral mapping techniques. Identified end-member spectra, including muscovite, kaolinite, and epidote were used for subsequent classification of hyperion data (Figure 10).

In this study, for mapping of the surface composition, the spectral angle mapper (SAM) was chosen. SAM is a physically-based classification algorithm that compares the spectral similarity between surface reflectance image spectra and reference spectra, treating them as vectors in a space with the dimensionality equal to the number of bands (Kruse et al., 1993; Jenson, 2005).

Spectral angle mapper (SAM) was performed to produce image map showing the distribution and abundance of selected minerals. Figures 12 and 13 illustrate SAM classification image maps produced for two selected subscenes consisting of Sarcheshmeh and Meiduk mines, showing spectrally predominant minerals as colored pixels.

The alteration minerals are represented as different colored pixels in Sar Cheshmeh/Seridune subset scene. Muscovite rich areas are as brown pixels and kaolinite as bluish green pixels. Epidote rich areas as pink pixels surround the circular to elliptical areas of hydrothermal mineral assemblages as it is shown in Figure 11. In Mieduk/Sara subset scene, muscovite rich areas are depicted as light green pixels, kaolinite as blue pixels. Epidote rich areas as red pixels surround the circular to elliptical areas of other alteration minerals (Figure 12).

We can assume that the SWIR spectra of muscovite (K Al_2 (Si Al_3) O10 (OH, F)$_2$ as indicator of phyllic alteration, kaolinite (Al_2 Si_2 O5 $(OH)_4$) as indicator of argillic alteration and epidote ($Ca_2(Al\ Fe^{3+})_3O\ (SiO_4)(SiO_7)(OH)$ as an indicator of propylitic alteration, respectively. Accordingly, hydrothermal alteration zones such as phyllic, argillic, and propylitic zones were discriminated using end-member spectra extracted directly from the hyperion image. Phyllic, argillic, and propylitic alteration zones were distinguished from one another and surrounding country rock, as well as the phyllic zone highlighted as indicator of high economic-potential area of copper mineralization in the two hyperion images.

The spatial distribution of identified hydrothermal alteration zones has been verified through *in-situ* inspection. The field photographs of the geomorphology, rock units, copper mines, and hydrothermal alteration zones are shown in Figure 13 (A-H). According to X-Ray diffraction (XRD) analysis of collected rock samples, the minerals predominantly were detected in the hydrothermal alteration zones included muscovite, illite, hematite and quartz in phyllic zone, kaolinite, montmorillonite and quartz in argillic zone, and epidote, chlorite, and quartz in propylitic zone. Figure 14 indicates the average spectra measurements of collected rock samples from hydrothermal alteration zones. The spectra of phyllic rock samples exhibit diagnostic absorption features at 2200 nm, Argillic rock samples at 2170 and

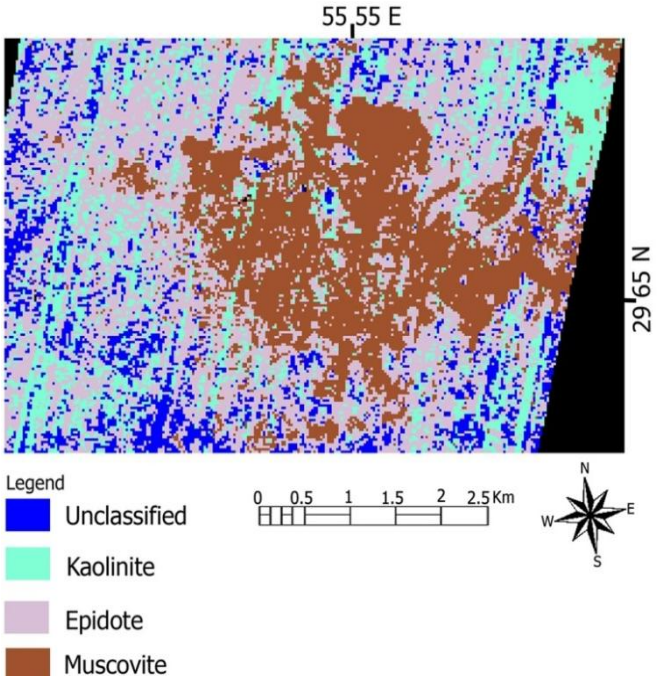

Figure 11. SAM classification mineral map for Sar Cheshmeh porphyry copper mine extracted from SWIR (2.0 to 2.4 µm) of hyperion data. Colored pixels show the spectrally predominant minerals in hyperion subscene.

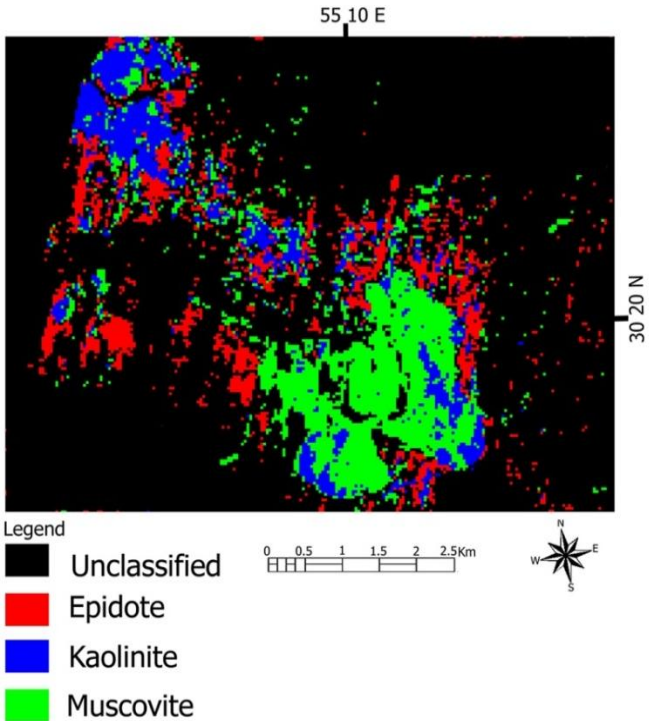

Figure 12. SAM classification mineral map for Meiduk mine extracted from SWIR (2.0 to 2.4 µm) of hyperion data. Colored pixels show the spectrally predominant minerals in hyperion subscene.

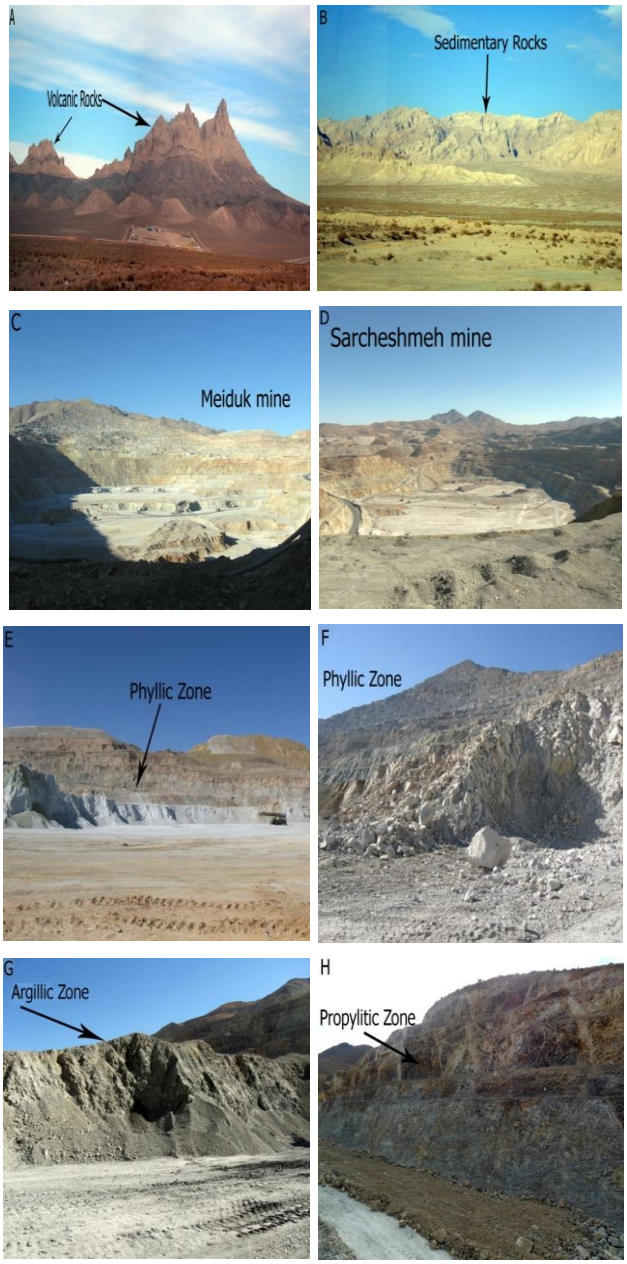

Figure 13. Field photographs of the study area. (A) Panoramic view of the volcanic rocks; (B) regional view of the sedimentary rocks; (C) Regional view of the open-pit quarry of Meiduk porphyry copper mine; (D) Regional view of the open-pit quarry of Sarcheshmeh porphyry copper mine; (E) View of the phyllic zone; (F) Close-up of the phyllic zone; (G) Argillic alteration zone; (H) Propylitic alteration zone.

2200 nm and propylitic rock samples at 2350 nm.

Conclusions

This paper investigates potential means to identify altered rocks and hydrothermal alteration zones associated with

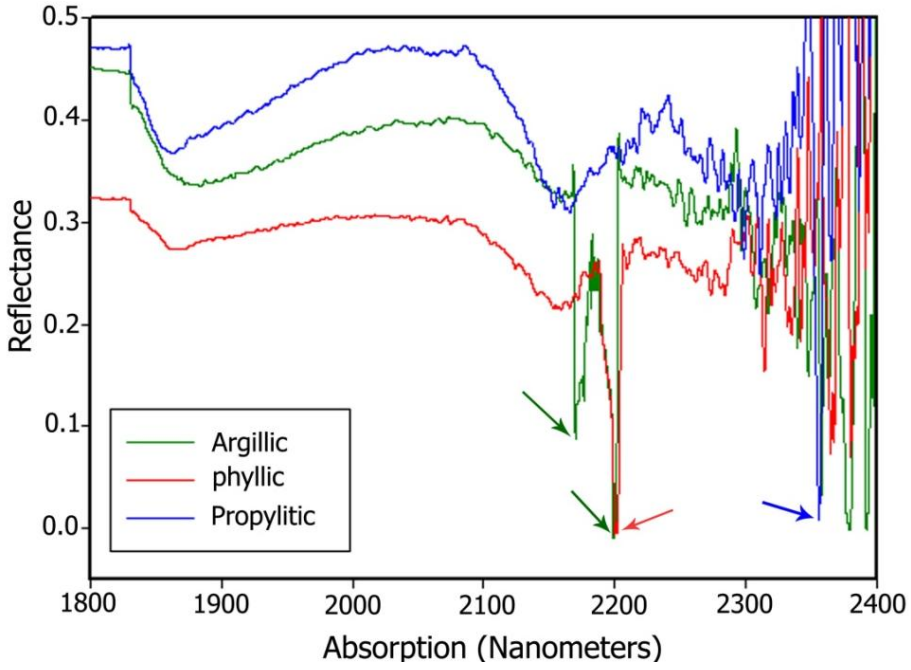

Figure 14. Laboratory reflectance spectra of altered rock samples, arrows pointed the maximum absorption. The average spectra of Phyllic rock samples has maximum absorption in 2200 nm; Argillic rock samples in 2170 and 2200 nm; Propylitic rock samples in 2350 nm.

porphyry copper mineralization using ALI and hyperion data in two copper mining districts in southeastern segment of the Central Iranian Volcanic Belt, Iran. A band ratio derived from ALI bands (4/2, 8/9, 3 in RGB) has been developed, allowing the identification of altered rocks, lithological units, and vegetation. AIG-Developed hyperspectral analysis methods produced image map of spectrally predominant minerals in alteration zones using hyperion shortwave infrared bands (Band 185 to Band 222). Three MNF transformed bands were employed to determine the end-members by pixel purity index (PPI) procedure and *n*-dimensional visualizer. A subset of identified end-members was used for spectral angle mapper (SAM) method. Minerals detected in the hydrothermal alteration zones included muscovite in phyllic zone, kaolinite in argillic zone, and epidote in propylitic zone. In this way, the spatial distribution of hydrothermal alteration zones such as phyllic, argillic, and propylitic were distinguished from one another and surrounding country rock. Results have proven to be effective, and in accordance with the results of field surveying, spectral reflectance measurements, and X-ray diffraction (XRD) analysis. This paper presented an approach to the extraction of spectral information from ALI and hyperion data for geological mapping and the detection of hydrothermal alteration zones for the reconnaissance stages of copper and gold at both regional and district scales.

ACKNOWLEDGEMENTS

This study was conducted as part of Tier1, Research University Grant Scheme, Ministry of Higher Education Malaysia. We are grateful to the *Universiti Teknologi Malaysia* for providing the facilities for this investigation. The authors would like to thank reviewers for their very helpful and constructive reviews of this manuscript.

REFERENCES

ACORN TM 5.0 (2004). Tutorial, ImSpec LLC, A dvanced Imaging and Spectroscopy, ImSpec LLC, pp. 67-70.

Alavi M (1994). Tectonic of the Zagros orogenic belt of Iran: new data and interpretations. Tectonophysics, 229: 211-238.

Amiraie A (1991). The study of mineralization and hydrothermal alteration at Meiduk porphyry copper deposit, M.Sc. thesis. Shiraz University. p. 125 (In Persian).

Beck R (2003). EO-1 User Guide, Version 2.3., University of Cincinnati.

Berberian F, Muir ID, Pankhurst RJ, Berberian M (1982). Late Cretaceous and early Miocene Andean type plutonic activity in Northern Makran and central Iran. J. Geol. Society London, 139: 605-614.

Boomeri M, Kazuo N, David RL (2009). The Meiduk porphyry Cu deposit, Kerman, Iran: A geochemical analysis of the potassic zone including halogen element systematics related to Cu mineralization processes. J. Geoche. Exploration, 103: 17-29.

Boardman JW (1993). Automated spectral unmixing of AVIRIS data using convex geometry concepts: in summaries, Fourth JPL Airborne Geoscience Workshop.

Chen CM (2000). Comparison of principal component analysis and Minimum Noise Fraction transformation for reducing the

dimensionality of hyperspectral imagery. Geo. Res., 33: 163-178.
Folkman M, Pearlman J, Liao L, Jarecke P (2001). EO-1/Hyperion hyperspectral imager design, development, characterization, and calibration. Hyperspectral Remote Sensing of the Land and Atmosphere, Proceedings of SPIE, 4151: 40-51.
Gad S, Kusky T (2007). ASTER spectral ratioing for lithological mapping in the Arabian–Nubian shield, the Neoproterozoic Wadi Kid area, Sinai, Egypt. Gond. Res., 11: 326-335.
Gersman R, Ben-Dor E, Beyth M, Avigad D, Abraha M, Kibreba A (2008). Mapping of hydrothermally altered rocks by the EO-1 Hyperrion sensor, northern Danakil, Eritrea. Int. J. Remote Sensing, 29(13): 3911-3936.
Green AA, Berman M, Switzer P, Craig MD (1988). A transformation for ordering multispectral data in terms of image quality with implications for noise removal: IEEE Trans. Geos. Remote Sensing, 26(1): 65-74.
Hassanzadeh J (1993). Metallogenic and tectonomagmatic events in the SE sector of the Cenozoic active continental margin of central Iran (Shahr e Babak area, Keman Province) [Ph.D. thesis]: Los Angeles, University of California, Los Angeles, p. 204.
Hearn DR, Digenis CJ, Lencioni DE, Mendenhall JA, Evans JB, Walesh RD (2001). EO-1 Avanced Land Imager overview and spatial performance. IEEE Transac.Geos.Remote Sensing. pp. 897-899.
Hezarkhani A (2006). Hydrothermal evolution of the Sar-Cheshmeh porphyry Cu–Mo deposit, Iran: Evidence from fluid inclusions. J. Asian Earth Sci., 28: 409-422.
Hubner H (1969a). Geological map of Iran sheet no. 5, southcentral Iran: Tehran, National Iranian Oil Company, scale 1:1,000,000.
Hubner H (1969b). Geological map of Iran sheet no. 6, southeast Iran: Tehran, National Iranian Oil Company, scale 1:1,000,000.
Hunt G (1977). Spectral signatures of particulate minerals in the visible and near infrared. Geophysics, 42: 501-513.
Hunt G, Ashley P (1979). Spectra of altered rocks in the visible and near infraraed. Econ. Geol., 74: 1613-1629.
Huntington JF (1996). The role of remote sensing in finding hydrothermal mineral deposits on Earth. Evolution of Hydrothermal Ecosystems on Earth (and Mars?). Wiley, England, pp. 214-234.
Inzana J, Kusky T, Higgs G, Tucker R (2003). Supervised classifications of Landsat TM band ratio images and Landsat TM band ratio image with radar for geological interpretations of central Madagascar. J. Afr. Earth Sci., 37: 59-72.
Kruse FA, Boardman JW, Lefkoff AB, Heidebrecht KB, Shapiro AT, Barloon PJ, Goetz AFH (1993). The Spectral Image Processing System (SIPS)–Interactive Visualization and Analysis of Imaging Spectrometer Data. Rem. Sensing Environ. 44: 145-163.
Kruse FA, Boardman JW (2000). Characterization and Mapping of Kimberlites and Related Diatremes Using Hyperspectral Remote Sensing. Proceeding. 2000 IEEE Aero-Space Conference, Big Sky, MO, March pp. 18-24.
Kruse FA Boardman JW, Huntington JF (2003). Comparison of airborne hyperspectral data and EO-1 Hyperion for mineral mapping. IEEE Transa. Geosc. Remote Sensing, 41(6): 1388-1400.
Kruse FA, Perry SL (2007). Regional mineral mapping by extending hyperspectral signatures using multispectral data. IEEE Trans. Geosc. Remote Sensing, 4: 1-14.
Mars JC, Rowan LC (2006). Regional mapping of phyllic- and argillic-altered rocks in the Zagros magmatic arc, Iran, using Advanced Spaceborne Thermal Emission and Reflection Radiometer (ASTER) data and logical operator algorithms. Geosphere, 2(3): 161-186.
National Aeronautics and Space Administration (2002). Earth Observing-1 Advanced Land Imager. Online: http://eo1.gsfc.nasa.gov/Technology/ALIhome1.htm
Pearlman JS, Barry PS, Segal CC, Shepanski J, Beiso D, Carman SL (2003). Hyperion, a Space-Based Imaging Spectrometer. IEEE Trans. Geos. Remote Sensing, 41(6): 1160-1173.
Pour BA, Hashim M, Marghany M (2011). Using spectral mapping techniques on short wave infrared bands of ASTER remote sensing data for alteration mineral mapping in SE Iran. Int. J. Phys. Sci., 6(4): 917-929.
Pour BA, Hashim M (2011a). Spectral transformation of ASTER and the discrimination of hydrothermal alteration minerals in a semi-arid region, SE Iran. Int. J. Phys. Sci., 6(8): 2037-2059.
Pour BA, Hashim M (2011b). Identification of hydrothermal alteration minerals for exploring of porphyry copper deposit using ASTER data, SE Iran. J. Asian Earth Sci., 42: 1309-1323.
Ranjbar H, Masoumi F, Carranza EJM (2011) Evaluation of geophysics and spaceborne multispectral data for alteration mapping in the Sar Cheshmeh mining area, Iran. Int. J. remote sensing, 32(12): 3309-3327.
Rockwell BW, Hofstra AH (2008). Identification of quartz and carbonate minerals across northern Nevada using ASTER thermal infrared emissivity data Implications for geologic mapping and mineral resource investigations in well-studied and frontier areas. Geosphere, 4(1): 218-246.
Shahabpour J (2005). Tectonic evolution of the orogenic belt in the region located between Kerman and Neyriz. J. Asian Earth Sci., 24: 405 -417.
Shahabpour J (2007). Island-arc affinity of the Central Iranian Volcanic Belt. J. Asian Earth Sci., 30: 652-665.
Shafiei B, Haschke M, Shahabpour J (2009). Recycling of orogenic arc crust triggers porphyry Cu mineralization in Kerman Cenozoic arc rocks, southeastern Iran. Min. Deposita, 44: 265-283.
Shafiei B (2010). Lead isotope signatures of the igneous rocks and porphyry copper deposits from the Kerman Cenozoic magmatic arc (SE Iran), and their magmatic-metallogenetic implications. Ore Geo. Rev., 37(1-2): 27-36.
Ungar SG, Pearlman JS, Mendenhall JA, Reuter D (2003). Overview of the Earth Observing One (EO-1) Mission. IEEE Transac. Geosci. Remote Sensing, 41(6): 1149-1159.
Waterman GC, Hamilton RL (1975). The Sarcheshmeh porphyry copper deposit. Econ. Geol., 70: 568-576.
Wulder MA, White JC, Goward SN, Jeffrey GM, Irons JR, Herold M, Cohen WB, Loveland TR, Woodcock CE (2008). Landsat continuity: Issues and opportunities for land cover monitoring. Rem. Sensing. Environ., 112: 955-969.